Monthly Notices of the ROYAL ASTRONOMICAL SOCIETY

MNRAS **507,** 90–103 (2021) https://doi.org/10.1093/mnras/stab2122
Advance Access publication 2021 July 23

Unveiling the nature of clusters in the Cygnus region. I. The embedded cluster DB2001–22

J. A. Molina Lera,[1★] R. Gamen,[2,3★] S. Cichowolski,[1★] G. Baume[2,3] and S. B. Cárdenas[1,3]

[1]*Instituto de Astronomía y Física del Espacio, UBA–CONICET, CC 67, Suc. 28, 1428 Buenos Aires, Argentina*
[2]*Instituto de Astrofísica de La Plata, CONICET–Universidad Nacional de La Plata, Paseo del Bosque S/N 1900, La Plata, Argentina*
[3]*Facultad de Ciencias Astronómicas y Geofísicas, UNLP, Paseo del Bosque S/N 1900, La Plata, Argentina*

Accepted 2021 July 18. Received 2021 July 18; in original form 2021 March 10

ABSTRACT

The Cygnus region harbours a vast diversity of rich stellar complexes. Hence, it is ideal for studying recently formed stellar clusters, and investigate how the feedback effect and radiation emitted by its massive stars modifies the interstellar medium giving place to induced star forming processes. This is the case of the small and poorly studied cluster DB2001-22. We focus our attention at analysing the cluster and its encompassing region, to distinguish different stellar populations and study their relationship with the surrounding environment. We gleaned literature and data bases for optical and IR photometry, astrometry provided by *Gaia* eDR3 and spectroscopy, and obtained new infrared Gemini spectra of three young stellar objects candidates (cYSOs). Furthermore, we detected two new massive stars: O7 V and B3 V, in the LAMOST data base, pointing out that DB2001–22 belongs to a much larger complex that involves an entire bubble structure and houses a richer massive population at a distance of 3.0 kpc. In this sense, DB2001–22 and the H II region G82.6+0.4 are clearly related. Some observed gas and dust structures seem to have been sculpted by these massive stars. Infrared emission is compatible with a hot ionized gas mixed with warm dust surrounded by a structured photo-dissociation region (PDR) scenario. We found nine Class I and 56 Class II cYSOs, whose distribution along the PDR and the tips of pillar structures suggests that their formation may have been induced by the action of the earliest stars in the cluster on to their environment.

Key words: stars: massive – stars: pre-main-sequence – ISM: bubbles – open clusters and associations: individual: DB2001–22 – galaxy: structure.

1 INTRODUCTION

The Cygnus region is located at $l \sim 80^{\circ}$ in the Galactic plane and it is just coincident with the inner extension of the Local Arm (Hou & Han 2014). In the past few years, this extension, has been reconsidered to be as relevant as the main Galactic arms and not just a spur (Reid et al. 2019; Shen & Zheng 2020; Zari et al. 2021). Due to its tangential directions, it harbours a vast diversity of rich stellar complexes that are seen superposed in the line of sight, but are in fact arranged at various distances (Bochkarev & Sitnik 1985; Odenwald & Schwartz 1993; Reipurth & Schneider 2008). Among these complexes there is evidence of OB associations, young embedded clusters, and bubble-like structures, massive star-forming regions, giant molecular clouds, and supernova remnants. It also harbours the well known Cygnus–X complex; one of the richest star-forming regions in the Galaxy, first detected by Piddington & Minnett (1952) and widely assumed to be located at a distance of 1.5–1.7 kpc (Schneider et al. 2006; Motte et al. 2007; Oskinova et al. 2010; Berlanas et al. 2018; Berlanas et al. 2020).

In this sense, the Cygnus region is ideal for selecting and studying small star-forming environments and link them to a larger scale. Hence, the thorough study of immersed clusters allows us to trace the different evolutionary states and outbreaks of star-forming which originates within a same molecular cloud. Under this scenario, a multiwavelength and multitechnique approach is useful to better estimate distances and intrinsic parameters, and to reach more accurate conclusions. Thus, in this work, we turned our attention to DB2001–22, a small and poorly studied embedded cluster located in the Cygnus area.

This paper is organized as follows: in Section 2, we present the studied region and previews results from the literature, in Section 3, we describe the used data, addressing the employed reduction procedures. In Section 4, we detail our analysis and results. Finally, in Sections 5 and 6, we present a general discussion of our analysis and conclusions.

2 DESCRIPTION OF THE REGION

DB2001–22 was first identified by Dutra & Bica (2001) as a partly resolved small cluster of 1.5–1.7 arcmin diameter in the radio H II region G82.6+0.4, and later catalogued as an IR star cluster by Bica, Dutra & Barbuy (2003) (see Fig. 1). It was studied by Kharchenko et al. (2013), using the PPMXL catalogue they estimated an age of $\sim$ 17 Myr and situate it at a distance $\sim$ 1.9 kpc with an $E_{(B-V)} =$ 2.228. Cantat-Gaudin et al. (2018), determined stellar components and distances using *Gaia* DR2, and established a most likely distance of 3369.2 pc.

★ E-mail: jalejoml@fcaglp.unlp.edu.ar (JAML); rgamen@fcaglp.unlp.edu.ar (RG); scicho@iafe.uba.ar (SC)

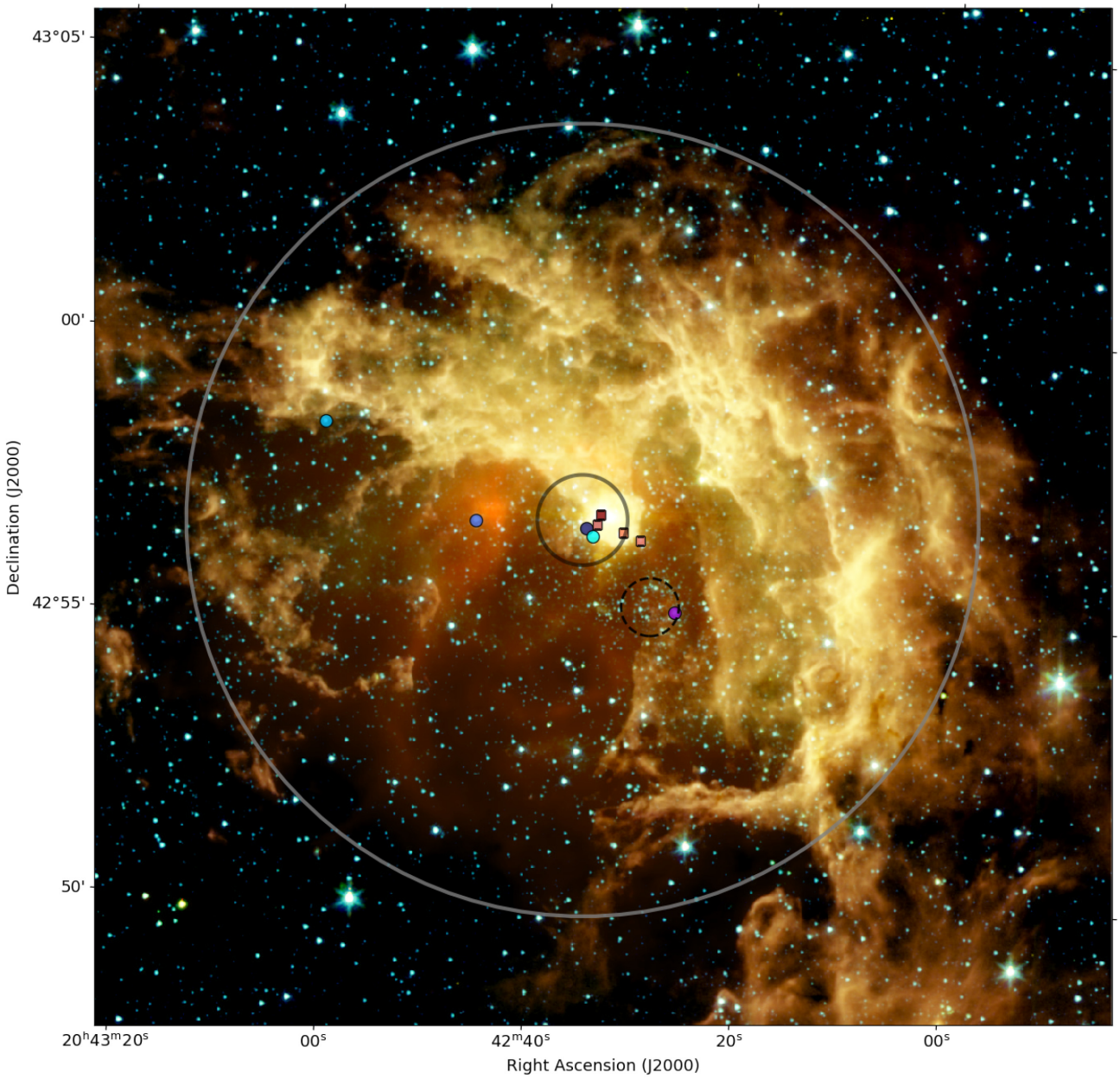

Figure 1. Colour image of *Spitzer* bands centred in the DB2001–22 position covering a region of 18 × 18 arcmin. Colours are represented as follows: blue (IRAC 1; 3.6 μm), green (I2; 4.5 μm), yellow (I3; 5.8 μm), red (I4; 8 μm), orange (MIPS1; 24 μm). The circumference, with a radius of 7′.0, delimit the studied region. The small black circumference represents the cluster size as established by Dutra & Bica (2001). The blue filled symbols, from darker to lighter tones, show in order from O6 to the B5, the four early-type stars (see Section 3.2.1). Also red squares represent, from darker to lighter tones target 0 to target 3 (see Section 3.2.2). The dashed circumference show a small group of stars, where the violet filled circle indicates a massive star candidate.

From the stellar-study point of view, Beerer et al. (2010) obtained optical spectra of OB-type candidates in a two-degree side field, which included DB2001–22. They identified two B-type stars, i.e. 2MASS J20403997+4253188 and J20423517+4256363. The former was classified as B5 ± 3. The other, was classified as B0 ± 2, in agreement with the oldest classification of Gehrz et al. (1980), i.e. B1–2 I. Nevertheless, its location coincides with the O6 IIIz (2MASS J20423517+4256363[1]) established by Berlanas et al. (2018), which they related to the surroundings of the Cygnus OB2 association at a distance of 1.4 kpc. By means of *Spitzer* data, Beerer et al. (2010) studied the Cygnus–X region, including the DB2001–22 area and made a census of massive stars and low–mass YSOs, to understand how low-mass stars form in molecular cloud complexes dominated by massive stars. They identified six clusters of cYSOs, being G82.55+0.40 one of them, coincident with the location in which DB2001–22 is immersed. The analysis was made assuming an unique distance of 1.7 kpc for the whole region.

On the other hand, *Spitzer* images of the DB2001–22 region revealed that the ISM has been strongly affected by the action of massive stars (see Fig. 1). These images shows several arc-like struc-

[1]In fact, they provided the ID 2MASS J20423509 + 4256364, which does not exist in the 2MASS database.

tures partially surrounding a cavity containing warm dust, and a very strong emission feature coincident with the position of DB2001–22. This region was associated with the IR source AFGL 2636 by Gehrz et al. (1980) who, based on IR and optical data, suggested that it is an active star-forming region. The MSX source G082.5682+00.4040, catalogued as a massive young stellar object (MYSO) candidate (Urquhart et al. 2009), is located over this bright region and it is the most probable responsible of the observed emission given that MYSOs are brightest in the IR, where most of their bolometric luminosity emerges after being reprocessed by the surrounding dust. Urquhart et al. (2009) associated G082.5682+00.4040 with the 6 cm VLA source G082.5677+00.4042, and classified it as a H II/YSO type, which means that the MSX source appears to be associated with both an H II region and a YSO.

The shell/bubble-like region was named G082.566+00.362 in the *WISE* catalogue of Galactic H II Regions (Anderson et al. 2014), with an assigned radius of 8.′5. The small and bright emission feature is also present in this catalogue as G082.567+00.405, with a 1.′4 size and indicated as a 'group H II region'. Both IR structures are identified as the IR counterpart of G082.582+00.411. Recently, using AKARI and Herschel data, Hanaoka et al. (2019) identified and analysed several shell-like IR bubbles, being this region one of them (named E21). They inferred a size of 5.′11.

In the radio domain, the area was first identified at 2695 MHz by Wendker (1970), who has established a 2 kpc lower limit to its distance. Later on, Normandeau, Joncas & Green (1992) detected it at 408 MHz using the DRAO Synthesis Telescope. They estimated the flux density and, combined with the one at 4850 MHz (Wendker 1984), confirmed the thermal nature of the emission.

Several radio recombination lines (RRL) were detected towards this region. Lockman (1989) distinguished the H87α and H88α 3 cm lines, while Balser et al. (2011) detected the H and He RRL.

The nature and origin of the embedded cluster DB2001–22 are not yet addressed, as well as the fact that its surrounding area presents very rich gas and dust structures. These structures suggest that the cluster and the different stellar populations within the area have influenced its local ISM. Thus, both, the cluster and its environment deserve further attention. Our first objective was to establish the region that encompass the stellar cluster and its environment to distinguish and characterize its different stellar populations. Moreover, we conducted a thought study in order to estimate its distance, colour excess (absorption), and age. In this sense, we intended to determine the location of the cluster within the structure of the Local Arm. We then analysed the relationship between these populations and their surrounding environment attempting to establish and study how different starbursts were originated within the environment and detect the sources responsible for creating the bubble, the knot and the pillars, and the arc-like structures seen at IR wavelengths.

3 DATA

3.1 Photometric and astrometric data

We used *ugri* images of the Sloan Digital Sky Survey (SDSS; Eisenstein et al. 2011) covering the region of DB2001–22 and its surroundings. These images were downloaded from the Science Archive Server (SAS[2]) already bias, dark, and flat corrected by the corresponding pipelines (Stoughton et al. 2002).

[2]https://dr12.SDSS.org/fields/

Table 1. Transformation equations and calibration coefficients used for SDSS observations together with the corresponding *rms* fit values.

Equation	*zp*	*c*	*rms*
$u_{\rm inst} = u + z$	6.77 ± 0.01	–	0.07
$u_{\rm inst} = g + z + c(g - r)$	6.82 ± 0.01	-0.01 ± 0.01	0.03
$r_{\rm inst} = r + z + c(r - i)$	6.82 ± 0.01	0.01 ± 0.01	0.02
$i_{\rm inst} = i + z + c(r - i)$	6.92 ± 0.01	-0.20 ± 0.01	0.04

Note. 'inst' subindex indicates instrumental magnitudes from PSF photometry.

We performed the photometric measurement over the SDSS images following a similar procedure used by Baume et al. (2020). Briefly, instrumental magnitudes were obtained using the point spread function (PSF) method (Stetson 1987) and the corresponding photometric tables were aperture-corrected for each filter to carry them to a final aperture size of 17 pixels (=6.73 arcsec) in radius. All resulting tables were combined using DAOMASTER code (Stetson 1992), obtaining a set for instrumental *ugri* bands. The flux calibration was performed using the information of about 150 common stars in the SDSS catalogue (Alam et al. 2015) and the IRAF/PHOTPARS package. In this procedure, we adopted the transformation equations presented in Table 1. In general, we considered a zero-point (*zp*) and a colour term. In the case of *u* band, only a zero-point was taken into account because some *u* sources with good signal-to-noise ratio (SNR) are saturated in the other bands. The fitted coefficients and the corresponding root-mean-square (*rms*) values are also indicated in Table 1. For saturated objects in SDSS images, we added, to the obtained calibrour ated catalogue, the *gri* bands from Pan–STARRS DR1 catalogue (Chambers et al. 2016), and a few stars from the SIMBAD data base *UBVRI* information transformed to SDSS photometric system using the equations given by Jester et al. (2005).

We also used proper motions and photometric data at *G*, G_{BP}, and G_{RP} bands, provided by the '*Gaia* Early Data Release 3' (eDR3; Collaboration 2020) and added the distances given by Bailer-Jones et al. (2021) derived from the *Gaia* eDR3.

Finally, we complemented the optical photometric data with the point sources catalogue of the 'Two Micron All Sky Survey' (2MASS; Skrutskie et al. 2006), the 'AllWISE data Release' (Cutri et al. 2012), and the catalogue from 'A *Spitzer* Legacy Survey of the Cygnus–X Complex'[3] (Hora et al. 2007). 2MASS provides photometric information at the *JHK* bands, the AllWISE catalogue at 3.6, 4.5, 5.8, and 8.0 μm bands, and the *Spitzer* catalogues have data at 3.6, 4.5, 5.8, and 8.0 μm (*ch*1, *ch*2, *ch*3, and *ch*4) bands.

3.1.1 *Final catalogue*

To obtain our final catalogue, we cross-correlated the point sources of the above indicated catalogues. In this procedure, we selected those point sources located in a region of 18 × 18 arcmin centred at the SIMBAD coordinates of DB2001–22 (α, δ)(*J*2000) = ($20^{\rm h}\ 42^{\rm m}\ 33.5^{\rm s}$, $42^\circ 56' 50''$). This region was identified as our working field of view (FOV; see Fig. 2). To manipulate and cross-correlate the tables we applied two different tools, the STILTS[4] and our own cross-correlation method (see Molina Lera, Baume & Gamen 2018), in order to verify the entire procedure. We considered the astrometric information provided by the World Coordinate System (WCS) of

[3]https://irsa.ipac.caltech.edu/data/SPITZER/Cygnus-X/
[4]http://www.star.bris.ac.uk/mbt/stilts/sun256/sun256.html

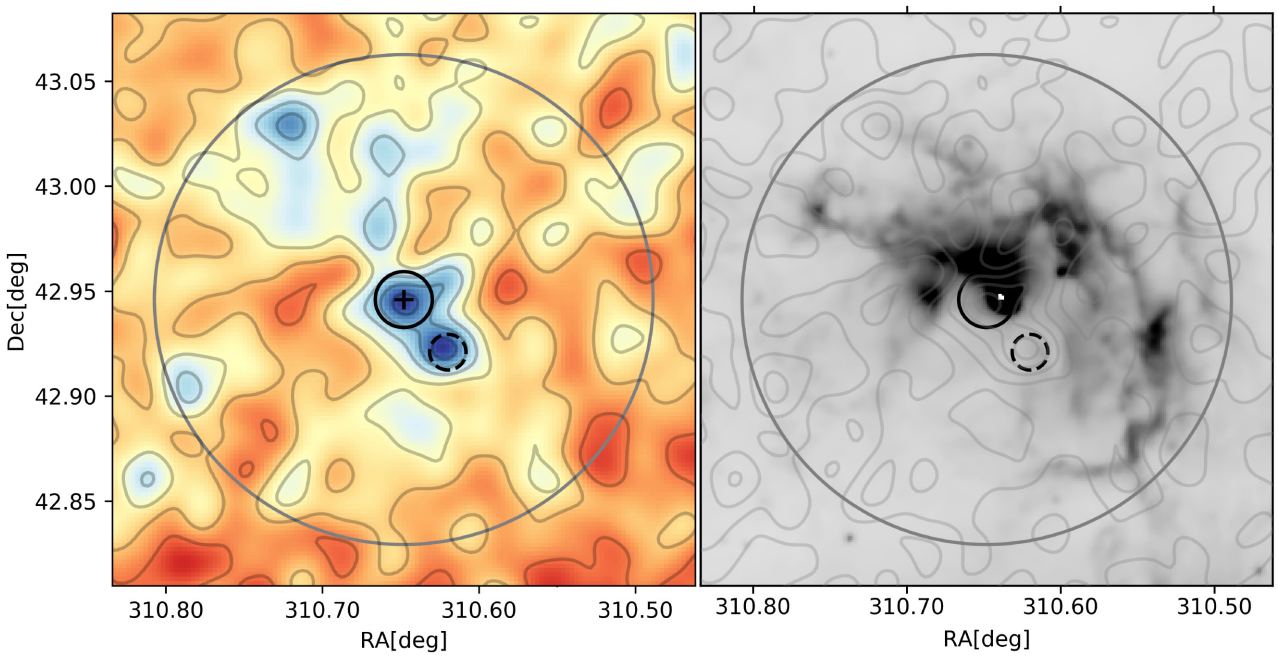

Figure 2. Figures centred in the DB2001–22 position covering a region of 18 × 18 arcmin. Left-hand panel: Stellar density map where the bluest colours indicate the highest density values. The right-hand panel presents a *WISE* 12 μm band image. The grey curves correspond to isodensity stellar values. The cross indicates the centre of BD2001–22. The black circles enclose the two maximum stellar density regions: one centred at DB2001–22 with a radius of 1.′6 according to Dutra & Bica (2001), the second one with a radius of 1.′0. The circumference, with a radius of 7.′0, delimits the studied region.

SDSS images and by each indicated catalogue. We obtained a catalogue with astrometric and photometric information (*ugri* + *JHK* + $W_1W_2W_3W_4$ + $GG_{BP}G_{RP}$ + *ch*1, *ch*2, *ch*3, *ch*4 bands) in the FOV. The photometric errors were those provided by the DAOPHOT, DAOMASTER codes, and the corresponding source catalogues. We present here only the firsts photometric lines in Table 2, the full catalogue is available online at the CDS.[5]

3.2 Spectroscopic data

3.2.1 Already existing spectra

We searched the SIMBAD data base for OB type stars and identified a O6 IIIz (2MASS J20423517+4256363; Berlanas et al. 2018) and a B5 V star (2MASS J20423446+4256291; Beerer et al. 2010). A B0 V was also detected by Beerer et al. (2010) which, in fact, resulted to be the same star that Berlanas et al. (2018) classified as an O6 IIIz.

Additionally, we conducted a search in the Large Sky Area Multi-Object Fiber Spectroscopic Telescope (DR5 v3 LAMOST[6]). This data base gives access to processed spectra, which have a wavelength coverage between ∼3800 and 9000 Å, and a reciprocal dispersion of about 1 Å px^{-1}, i.e. suitable for spectral classification in the MK system. Thus, we downloaded hundreds of files for visual inspection and identified three early-type spectra (see Table 3).

3.2.2 New near-infrared spectra

We selected sources with probable IR excess located in the centre of the knot or pillar structure. Thus, we acquired near-IR spectroscopic data, upon a pre-selection of targets.

Observations were carried out using the GNIRS mounted at Gemini North (Program ID: GN-2017A-Q-12; PI: JAML) in its low-resolution mode. We employed a 0.675 arcsec slit, the 31.7 l/mm G5533 grating, centred at 2.11 μm, hence we obtained a useful wavelength coverage between 2.0 and 2.4 μm, with a spectral resolving power $R \sim 900$ at 2.1 μm.

We secured two observations, one centred on the G082.5682+00.4040 IR source (target 0), the other positioned to include the targets: 2MASS 20423406+4256411 (target 1) and 2MASS 20422985+4256257 (target 3). An extra target was also present in the slit, we identified it as 2MASS 20423156+4256333 (target 2). A telluric standard (HIP 103108; A1 V) was observed immediately after to be subtracted, as also calibrations (Ar–lamps, flats, etc.). We used PYRAF packages and the Gemini Observatory instructions to perform the reduction procedure. One of the pointings needed an exposure of five minutes, which resulted highly contaminated by the sky emission. In this case, we preferred to extract the spectra by using the APALL task; extracting the sky (background) spectrum on parallel strips close to the source position. Nevertheless, as it is shown below, these spectra are still contaminated by sky emission.

3.3 Radio and infrared image data

We complemented our data, with the information available in the Canadian Galactic Plane Survey (CGPS; Taylor et al. 2003). This survey provides 1420 MHz radio continuum data with 1.′0 angular resolution and a *rms* noise of 0.05 K.

We downloaded IR images from the survey 'A *Spitzer* Legacy Survey of the Cygnus-X Complex', this project survey a 24 deg^2 region with the IRAC 3.6, 4.5, 5.8, and 8.0 μm bands and MIPS 24 and 70 μm bands to study the relatively nearby active region of massive star formation (Beerer et al. 2010). The resolution of the

[5] http://simbad.u-strasbg.fr/simbad/
[6] http://dr5.lamost.org/

Table 2. Optic and IR photometric catalogue sample. The full version is available online at the CDS.

id	RAJ2000	u	g	r	i	J	H	K	W1mag	W2mag	W3mag	W4mag	Gmag	BPmag	RPmag	i1mag	i2mag	i3mag	i4mag
	DEJ2000	e_u	e_g	e_r	e_i	e_J	e_H	e_K	e_W1mag	e_W2mag	e_W3mag	e_W4mag	e_Gmag	e_BPmag	e_RPmag	i1mage	i2mage	i3mage	i4mage
1	310.527635	14.8293	12.0865	10.588	9.8226	8.643	8.055	7.863	7.736	7.871	6.759	4.037	10.733374	11.500271	9.881401	7.856	7.948	7.787	7.683
	42.876156	0.004	0.009	0.0413	0.0682	0.029	0.02	0.018	0.026	0.02	0.03	0.042	0.002761	0.002856	0.003785	0.015	0.015	0.016	0.029
2	310.584999	15.3533	13.9384	13.4479	13.2247	12.288	11.938	11.82	11.59	11.649	8.643	6.531	13.468022	13.83845	12.924099	11.818	11.855	11.686	11.401
	43.050860	0.0057	0.004	0.0011	0.0002	0.021	0.022	0.019	0.027	0.028	0.03	0.088	0.002759	0.002917	0.003804	0.017	0.017	0.054	0.155
3	310.719021	15.6043	14.2715	13.8272	13.5934	12.712	12.409	12.395	12.493	12.981	11.067	8.85	13.839488	14.186755	13.326808	12.374	12.418	12.363	12.435
	43.005037	0.0061	0.0071	0.005	0.0021	0.022	0.022	0.02	0.066	0.28	–	–	0.002761	0.002912	0.003813	0.02	0.024	0.175	1.021
4	310.661189	15.7533	14.3739	13.8542	13.6493	12.765	12.411	12.294	10.821	11.235	5.406	0.715	13.90949	14.270162	13.379787	12.303	12.236	–	–
	42.960773	0.0065	0.0068	0.014	0.0052	0.022	0.022	0.019	0.024	0.035	0.101	0.05	0.002794	0.003179	0.00407	0.03	0.031	–	–
5	310.726479	16.1183	14.7102	14.1307	13.8008	12.701	12.365	12.312	11.778	11.574	7.646	3.459	14.126892	14.550252	13.52154	12.177	12.119	12.007	–
	42.897879	0.0079	0.0034	0.0099	0.0027	0.027	0.033	0.036	0.029	0.036	0.055	0.076	0.002761	0.003043	0.003919	0.019	0.019	0.064	–
6	310.639793	16.7573	14.8832	14.0625	13.7083	12.366	11.949	11.842	11.604	11.443	7.943	5.926	14.071836	14.65003	13.342232	11.795	11.827	11.884	11.943
	43.056028	0.0152	0.0053	0.003	0.0038	0.023	0.021	0.021	0.029	0.034	0.029	0.082	0.002761	0.002931	0.00382	0.019	0.019	0.133	0.738
7	310.696525	16.8693	15.1572	14.3042	13.8984	12.616	12.176	12.03	11.658	11.81	10.593	8.679	14.299793	14.883162	13.563065	12.006	12.014	12.036	12.273
	42.908551	0.012	0.0044	0.0026	0.006	0.025	0.03	0.023	0.027	0.042	–	–	0.002762	0.002986	0.003837	0.017	0.018	0.048	0.178

IRAC bands are better than 2 arcsec, while the MIPS 24 and 70 μm band have a resolution of 6 and 18 arcsec, respectively. We also used the 12 μm image obtained from the *Wide-Field Infrared Survey Explorer* (*WISE*) which presents an angular resolution is 6.″5.

4 ANALYSIS AND RESULTS

As shown in Fig. 1, the region under study is composed of the embedded cluster, different stellar populations and gas/dust, all immersed in a bubble-like structure. Thus, the analysis and calculation of the parameters, regarding the stellar components of the cluster and its surroundings, were conducted following the main guidelines described in our previous works (Molina Lera et al. 2018; Molina Lera, Baume & Gamen 2019). In turn, the gas/dust structures were studied first in relation to their morphology and distance to the region, and then estimating their physical parameters as done in other similar structures (Cichowolski et al. 2015, 2018).

4.1 The stellar population at DB2001–22

We constructed a stellar density map of the region by means of the statistical function provided by PYTHON[7] package 'SCIPY STATS GAUSSIAN KDE'.[8] This map was built across an area of 18 × 18 arcmin using only the brightest sources ($K < 15$) in the 2MASS point sources catalogue, as shown in Fig. 2. Hence, we were able to study the stellar density distribution and detected two main peaks: one of them centred at DB2001–22, and the other at 1.′7 to the south–west (SW) of this location. Since the stellar population exceeds the size of the knot, we widen our selection in order to enclose the bubble-like structure. Accordingly, we conducted the study within a circumference centred in the coordinates of DB2001–22 with a radio of 7.′0 (see Fig. 1).

The distance was determined by applying three mainly independent techniques: spectroscopic calculations, photometric estimations, and the use of geometric distance estimations based on *Gaia* eDR3. Colour excesses and absorption were estimated by means of spectroscopic/photometric calculations and photometric estimations. The age was inferred considering the evolutionary state of the most massive member located in the main sequence (MS), and by comparing the location of a set of isochrones to the distribution of the photometric data. In all cases, we used a normal value for the total to selective extinction ratio $R_V = 3.1$ (see Section 5).

4.1.1 Spectroscopic classification and analysis of the OB population

We classified the three LAMOST spectra based on Walborn & Fitzpatrick (1990) as this atlas provides B-type standards for comparison. Due to the low SNR value in the spectra (see Table 3) classification should be considered as preliminary and in some cases follow-up observations might be convenient.

We identified HeII absorption lines in the LAMOST source J204245.76+425642.1, i.e. HeII λ4542, 4686, 5412, and 6891. Also, absorption lines of HeI λ4471, 4713, 5015, 5875, 6678 (blended with HeII λ6683?) and 7066. In addition, we noted the presence of the Hα, Hβ, Hγ, and Hδ Balmer series (and some lines of the Paschen one). Hα has a narrow emission component superimposed to the absorption. Regarding the almost similar intensities of the

[7] http://www.python.org

[8] https://docs.scipy.org/doc/scipy/reference/generated/scipy.stats.Gaussian_kde.html

Table 3. LAMOST sources identified as OB-types in this work. In successive columns, we show keywords given by the LAMOST data base, i.e. the name adopted in the LAMOST survey (desig), the cross-matched source in 2MASS (2MASS id), coordinates in *J*2000.0 equinox (α and δ), date of observation (date–obs), the spectral type provided (SUBCLASS), the signal-to-noise ratio (SNR*g*), our new spectral type determined (new sptype) and the geometric distance determined by Bailer-Jones et al. 2021.

LAMOST desig	2MASS ID	α	δ	SUBCLASS	SNR g	new sptype	*Gaia*–dist
J204245.76+425642.1	J20424577+4256421	310.690707	42.945036	Non	17.54	O7–7.5 V	$3.28^{+0.15}_{-0.16}$
J204300.60+425821.8	J20430061+4258218	310.752535	42.972742	A0III	26.86	B3 V	$2.68^{+0.24}_{-0.22}$
J204302.88+425648.5	J20430288+4256485	310.762001	42.946815	A0	113.99	B7 V	$1.40^{+0.03}_{-0.03}$

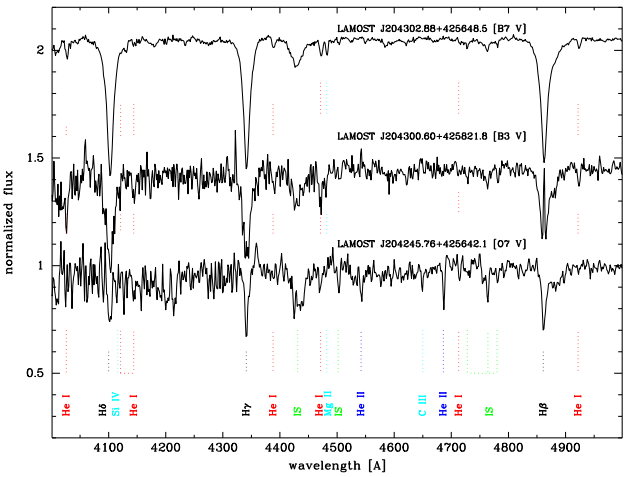

Figure 3. LAMOST spectra of the three OB stars detected in the area. Note the H β component in emission in the B3-type star.

HeI λ4471 and He II λ4542, we compared the LAMOST spectra with the standards of O7 and O8 sub-types, HD 97966 (O7 V) and HDE 305539 (O8 V). In despite of the low SNR of the LAMOST spectrum, its characteristics show a greater similarity with the O7 subtype. The only rarity is the C III λ4647/50/51 blend, it is stronger than expected in a O7 sub-type. Nevertheless, it should be similar to HeII λ4542, if O8, which clearly is not the case. Higher luminosity classes are rejected as no emission lines are detected. Thus, we classify it as O7–7.5 V.

The remaining two LAMOST spectra were mainly classified taking into account the intensities of the He I absorption lines, which reach the maximum at B2. For stars later than B2, we considered the strength of Mg II λ4481. Our spectral classifications are shown in Table 3, and the corresponding spectra are depicted in Fig. 3.

We calculated the spectroscopic distances to the five OB stars (the three discovered in LAMOST data base and the other two known ones). Absolute visual magnitude and intrinsic colour calibrations for MS were adopted from Sung et al. (2013) and transformed to the SDSS photometric system according to the equations given by Jester et al. (2005). For IR photometric calibration we used the MS given by Koornneef (1983) and Sung et al. (2013). For spectral types not included in these works, we performed a linear interpolation. Colour excess $E_{(B-V)}$, for each star, was estimated computing the colour excesses at *grJHK* bands, transforming them using the relative absorption values given by Cardelli, Clayton & Mathis (1989) and averaging the corresponding results. This obtained $E_{(B-V)}$ was used to compute the corresponding spectroscopic distance. Table 4 shows the results along with the adopted spectral types from which we performed the spectroscopic/photometric calculations, and the distance derived from *Gaia* (see below), just for comparison.

For the source J20423446+4256291 (type B5 ± 3), we conducted the spectroscopic/photometric calculation from a B2 V to a B8 V, taking into account the errors stated by Beerer et al. (2010). Considering these results and its position in the photometric diagrams (see Fig. 4), we finally adopted it as a B3 V. We discarded J20430288+4256485 (B7 V) since its derived distance (both by our calculations and by *Gaia*: $d \sim 1.5$ kpc), indicates it is not member of DB2001–22. Employing the remaining four stars, we obtained a mean distance of 3.0 ± 0.2 kpc and $E_{(B-V)} = 1.94 \pm 0.19$ mag, thus an absorption (A_V) $A_V = 6.02 \pm 0.57$.

4.1.2 *Photometric analysis*

We constructed photometric two-colour diagrams (TCDs) and colour–magnitude diagrams (CMDs). The upper main sequence (UMS) was identified by selecting sources which appear to be earlier than A0, simultaneously on the $(u-g)$ versus $(g-r)$ and the g versus $(u-g)$ diagrams. As a result of this procedure, the selection of the four UMS stars was coincident with the four OB–type stars analysed in Section 4.1.1.

To estimate the photometric distance and colour excesses, we compared the position of the UMS stars to the reference calibrations for the zero age main sequence (ZAMS) given by Sung et al. (2013) and Koornneef (1983). Sung et al. (2013) calibrations were transformed to the SDSS photometric system according to the equations given by Jester et al. (2005). The age of the cluster was inferred from the presence of the O7 V star evolutionary state. Thus, an upper limit of ∼8 Myr (Meynet, Mermilliod & Maeder 1993; Ekström et al. 2012) can be stated with confidence. We also estimated the age by comparing, in the g versus $(u-g)$ CMD, a set of solar metallicity isochrones for post-main sequence stellar populations (Bressan et al. 2012), to the UMS star distribution, obtaining a value of 10–32 Myr.

We considered a typical error in the estimated distance modulus of 0.2 mag. Thus, we derived a distance of 3.0 ± 0.3 kpc and a colour excess $E_{(B-V} = 1.9$ ($A_V = 5.9$). The TCDs and CMDs photometric diagrams are shown in Fig. 4, where we also included the reddening law, the ZAMS, MS, and isochrones and the positions of the four UMS stars.

In turn, given the location where the second stellar density peak was detected (see Fig. 2), its stellar population could be related to the knots cometary structure in which the embedded cluster is immersed. For this reason, we distinguished the source 2MASS J20422635+4255099 (identified in Figs 1 and 7 with a violet circle) and based on its location in the optical and near-IR photometric diagrams we pointed out as a massive star candidate.

To look for young stellar object candidates (cYSOs) we used the point-source IR catalogues provided by the *WISE* and *Spitzer* missions. To this aim, we applied the colour criteria described in Koenig et al. (2012) and Gutermuth et al. (2009) to the *WISE*

Table 4. Main parameters of stars with spectral type used in the spectroscopic distance determination. The successive columns indicate: the 2MASS source name, its spectral type, the ST assigned for the calculations, the $E_{(B-V)}$ calculated through the bands in the superscript, their colour excess and absorption mean values, the spectroscopic distance, and the geometric distance determined by Bailer-Jones et al. (2021).

2MASS Id	ST	ST_a	$E_{(B-V)}$				$\overline{E_{(B-V)}}$	$\overline{A_V}$	SP–dist	*Gaia*–dist
			$E_{(g-r)}$	$E_{(J-K)}$	$E_{(J-H)}$	$E_{(H-K)}$	(mag)	(mag)	(kpc)	(kpc)
Probable members										
20430061+4258218	B3V	B3V	1.78	1.60	1.70	1.41	1.62	5.02	3.04	$2.68^{+0.24}_{-0.22}$
20423446+4256291	B5 ± 3V	B3V	2.11	2.06	2.08	1.97	2.06	6.39	2.75	$2.74^{+0.25}_{-0.24}$
20423517+4256363	O6IIIz	O6III	2.00	2.06	2.08	2.02	2.04	6.32	2.98	$1.98^{+0.85}_{-0.64}$
20424577+4256421	O7V	O7V	2.26	1.99	2.08	1.82	2.04	6.32	3.20	$3.28^{+0.15}_{-0.16}$
Non-members										
20430288+4256485	B7V	B7V	0.89	0.98	1.06	0.86	0.95	2.95	1.08	$1.40^{+0.03}_{-0.03}$

and *Spitzer* sources, respectively, using stars with photometric flux uncertainties < 0.2 mag. in all bands.

We found 371 *WISE* and 256 *Spitzer* sources that fulfil this selection criteria. Before attempting to identify the cYSOs, we selected the non–YSO sources with excess IR emission, such as PAH–emitting galaxies, broad-line active galactic nuclei (AGNs), unresolved knots of shock emission, and PAH–emission features. Then, a total of 252 and 17 *WISE* and *Spitzer* sources, respectively, were dropped from the lists. Among the remaining 119 *WISE* and 239 *Spitzer* we look for both, sources with IR emission arising mainly from a dense in–falling envelope, including flat spectrum objects (Class I sources), and pre–MS stars with optically thick discs (Class II sources). We finally found nine sources (2 *WISE* and 7 *Spitzer*) identified as Class I cYSOs and 56 (16 *WISE* and 40 *Spitzer*) as Class II sources. They are listed in Table 5 and their spatial locations are indicated in Fig. 7. In particular, the *Spitzer* #1 coincides with MSX G082.5682+00.4040.

In order to estimate the level of contamination in the cYSOs detection, we applied the same colour criteria to the IR sources lying in a nearby control region, that shows no significant IR emission structures. We found 177 *WISE* and 514 *Spitzer*, with good photometric qualities. Among them, 13 (6 *WISE* and 7 *Spitzer* sources) are classified as Class II cYSOs and none as Class I. Thus, the number of cYSOs found outside the ionized region is much lower, suggesting that contamination in our studied area is low.

4.1.3 Astrometric analysis

Information provided by *Gaia* eDR3 was used to estimate the cluster distance. The sources were selected considering relative error bounds in proper motion ($e_{\rm pm} < 0.2$ pm) and distance ($e_{\rm dist} < 0.3$ dist) as given by Bailer-Jones et al. (2021) as well as their location in the vector point diagram (μ_δ, $\mu_\alpha \cos\delta$). For this purpose, we took into account the main guidelines regarding proper motion analysis indicated by Baume et al. (2011). Nineteen *Gaia* sources fulfilled these constraints, only one star (2MASS J20424871+4258073) was detected as an outlier, due to its nearer distance (∼1.4 kpc) and removed from the analysis. Individual distances were used to calculate an error weighted average. We obtained a mean distance of $3.0^{+0.6}_{-0.4}$ kpc.

Regarding the four near-IR sources situated at the knot or pillar, for which we obtained GNIRS spectra (see Section 4.2), we noticed that, except for target 2 ($d = 0.51 \pm 0.01$ kpc), all other three sources appear to be at the cluster distance. The target 0 has a distance $d = 3.6^{+1.2}_{-0.6}$ kpc. Target 1 ($d = 4.5^{+2.4}_{-1.4}$ kpc), and target 3 ($d = 2.8^{+2.8}_{-0.9}$ kpc) were not selected in this analysis due to their large error values and the reported problems regarding parallaxes of objects with emitting circumstellar material or high-brightness nebulously (Kimeswenger & Barría 2018). Additionally, the established distance for the source pointed out as a massive star candidate 2MASS J20422635+4255099 (see Section 4.1.2), was calculated in 3.1 ± 0.3 kpc.

4.2 Spectral analysis of sources in the pillar

As explained in Section 3.2.2, we secured two pointings, i.e. one centred in the YSO G082.5682+00.4040 (target 0 in this work) and other including two sources in the slit (an additional third spectrum was also present in the 2D spectral image, thus it was extracted). These three sources are identified as 2MASS J20423406+4256411 (target 1), J20423156+4256333 (target 2), and J20422985+4256257 (target 3). The obtained spectra are shown in the Fig. 5.

In target 0, we identified Br γ in emission as unique feature, this line is frequently seen in YSOs (Ishii et al. 2001). As no other lines are detected, as for example H_2 or CO, it could be classified as a low-mass YSO. This source is the same observed in the RMS Survey (Lumsden et al. 2013). There, in the published spectrum (viewable as PNG), H, He I, Fe II, H_2, and CO emissions are labelled, but only H, Fe, and He seems reliable. Thus, although our own spectrum does not confirm it, the source could be an intermediate- to high-mass YSO.

The target 1 presents conspicuous CO absorption bands, a weak Br γ (contaminated by the sky emission), SiI 2.25438 μm and MgI 2.28142 μm. The spectrum is contaminated at the position where Ca lines should be located. According Wallace & Hinkle (1997), CO bands are present between K–M stars and Br γ decreases its intensity towards later types, we tried to classify it in the early-K dominion. We make use of the atlas published by Rayner, Cushing & Vacca (2009), noting the weakness of Br γ and the lack of any feature between the first two ^{12}CO bands, i.e. no Na I nor ^{13}CO, a early K-type giant seems to be suitable. Lastly, making use of the quantitative calibration of Ghosh et al. (2019) for K–M giants, i.e. related to the equivalent widths (EW) of ^{12}CO (2–0) and (3–1), we measured about 9.5 and 6.5 Å, respectively, thus implying a K0 III star.

In the spectrum of the target 2, we only identified Br γ in absorption, indicating an A type. While the spectrum of the target 3 resembles the target 1 one. It has intense CO absorption bands, but the triplet Ca I is clearly identified and no Br γ is detected. Besides, it seems to be present the emission line of H_2 at 2.1218 μm. Considering the same facts as in the target 1, a K0-1 III spectral type is determined. In this spectrum, the EW of ^{12}CO(2–0) resulted larger (∼10.5 Å) but the one of (3–1), smaller (∼5.5 Å).

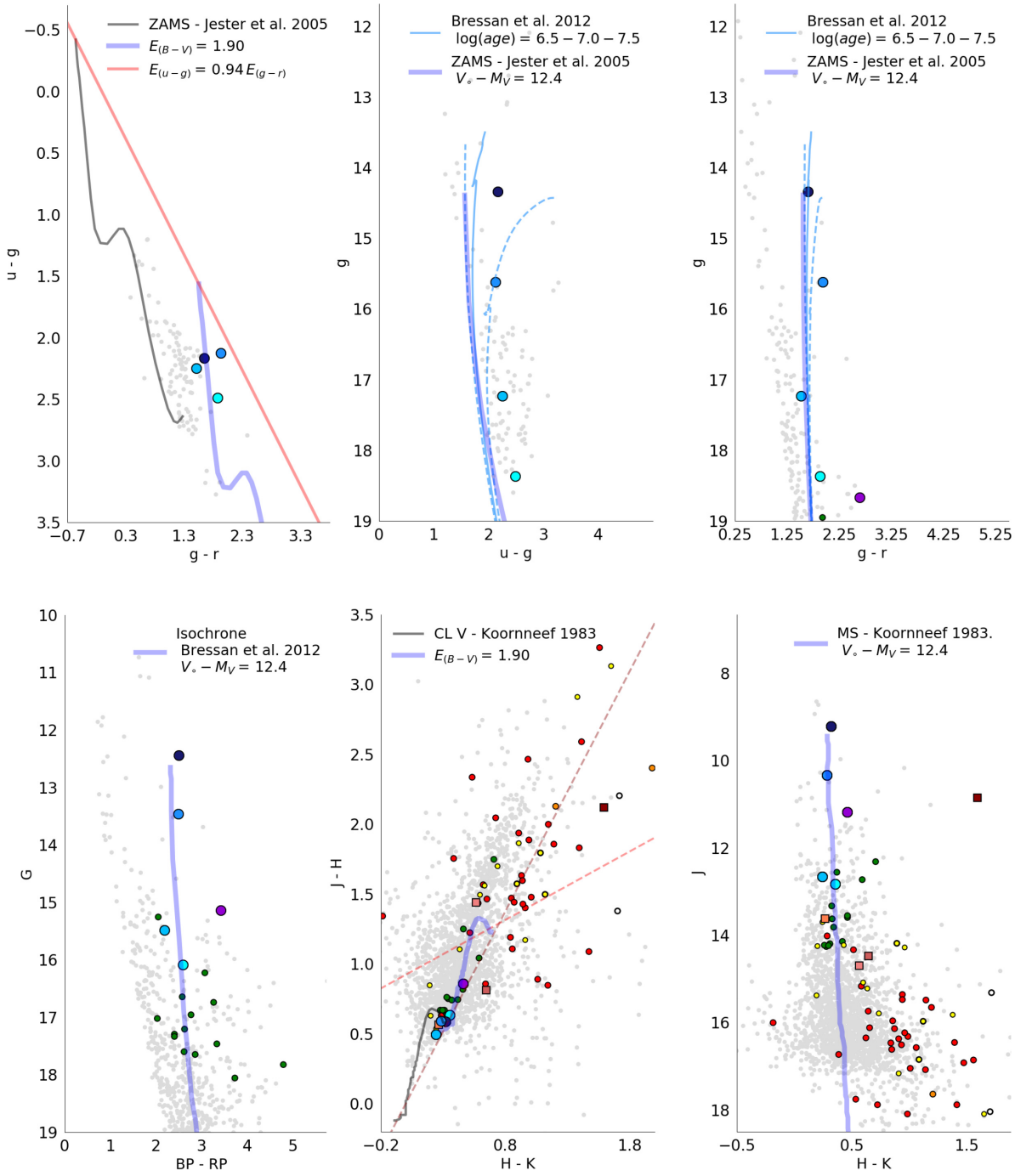

Figure 4. Photometric diagrams of sources in the defined working area. The black and blue curves correspond to MS or ZAMS reference stars. Continuous red lines represent the reddening direction. The red dotted lines show Meyer, Calvet & Hillenbrand (1997) criterion. Bressan et al. (2012) isochronous are shown as light blue curves. The blue filled circles, from darker to lighter tones, show in order the UMS from O6 to the B5, the four early-type stars. Also red squares represent, from darker to lighter tones target 0 to target 3. The red and orange circles represents YSOs class I and II candidates, respectively. The green squares are stars selected from the *Gaia* data analysis.

Both spectra – targets 1 and 3 – were included and classified for completeness but considered as non-members, i.e. most likely unrelated contamination. Nevertheless, they cannot be entirely ruled out as YSOs or PMS stars, since other works classified as low-mass young stellar objects, sources without the presence of emission lines (Greene & Lada 1996; Doppmann et al. 2005).

4.3 The ISM local to DB2001–22

We analysed the distribution and characteristics of the gas and dust present in the DB2001–22 surroundings, aiming to investigate the role that the stellar components had in perturbing the ISM.

As mentioned in Section 1, several RRLs have been detected towards the ionized region, at velocities of -9.6 ± 1.1, -13.91 ± 0.11, and -15.47 ± 0.72 km s^{-1} (Lockman 1989; Balser et al. 2011).

Table 5. YSO candidates obtained from *WISE* and *Spitzer* catalogues. The column (Notes) indicates its coincidence with other source detected and which group the cYSO belongs to. The last three columns represent the geometric distances determined by Bailer-Jones et al. (2021) (median, low, and high).

				Spitzer sources							
#	Designation	α (deg.)	δ (deg.)	3.6 μm (mag)	4.5μm (mag)	5.8 μm (mag)	8.0 μm (mag)	Notes	*Gaia*–dist	lo (kpc)	hi
					Class I						
1	J204233.77+425651.3	310.640688	42.94758	5.661	4.745	3.908	2.91	MSX G082+00.4 (i)	3.63	2.91	4.8
2	J204222.82+425556.8	310.595093	42.932457	13.115	12.403	11.662	10.778	(ii)	–	–	–
3	J204224.10+425731.7	310.600433	42.958801	8.69	7.975	7.012	5.992	WISE #48 (iii)	–	–	–
4	J204223.68+425733.2	310.598663	42.959225	11.323	9.91	8.789	7.561	WISE #48 (iii)	–	–	–
5	J204222.48+425743.8	310.593658	42.962166	11.174	10.032	9.068	8.34	WISE #49 (ii)	–	–	–
6	J204214.24+425338.7	310.559326	42.894081	11.021	9.964	9.098	8.045	(iii)	–	–	–
7	J204200.23+425350.7	310.500946	42.897423	12.211	10.826	9.913	9.367	(v)	–	–	–
					Class II						
8	J204234.03+425516.2	310.641756	42.921176	11.262	10.925	10.611	10.135	(iv)	2.15	1.11	3.99
9	J204232.87+425558.4	310.637371	42.932634	12.872	12.384	11.873	11.393	(iv)	2.88	1.64	4.98
10	J204236.64+425538.6	310.652649	42.927383	14.457	14.043	13.462	12.855	(iv)	–	–	–
11	J204228.81+425539.0	310.619633	42.927266	13.341	13.052	12.596	11.488	(iv)	3.71	1.91	7.61
12	J204229.05+425504.4	310.620998	42.917924	12.475	12.24	11.872	10.499	(ii)	2.42	1.58	4.06
13	J204237.90+425538.8	310.657898	42.927448	13.824	13.553	13.372	12.663	(iv)	–	–	–
14	J204228.27+425535.0	310.617737	42.926424	11.854	11.465	11.185	10.381	(iv)	3.07	1.87	4.46
15	J204228.57+425551.9	310.619019	42.931084	13.875	13.539	13.144	12.745	(iv)	–	–	–
16	J204238.76+425552.9	310.661499	42.931362	13.589	13.289	12.722	11.683	(iv)	–	–	–
17	J204227.14+425542.4	310.613068	42.928444	13.244	12.864	12.539	12.028	(iv)	–	–	–
18	J204228.91+425436.6	310.620453	42.910168	12.991	12.404	11.935	10.971	(ii)	–	–	–
19	J204227.55+425451.4	310.614789	42.914273	12.08	11.896	11.604	11.002	(ii)	4.19	2.88	6.38
20	J204226.40+425550.6	310.609985	42.93071	13.771	13.236	12.885	12.143	(iv)	–	–	–
21	J204235.09 + 425410.4	310.646165	42.902906	12.422	11.758	11.081	10.099	(iv)	3.92	1.68	6.54
22	J204237.03+425416.7	310.654235	42.904598	12.734	12.13	11.492	10.373	(iv)	4.17	2.53	5.44
23	J204226.51+425606.9	310.610474	42.935261	13.142	12.697	12.397	11.86	(iv)	–	–	–
24	J204235.91+425406.7	310.649627	42.90187	12.797	12.422	12.032	11.276	(iv)	2.34	1.16	5.1
25	J204228.88+425701.3	310.620331	42.950375	12.727	12.225	11.725	10.442	(iv)	–	–	–
26	J204223.56+425521.0	310.598175	42.922512	12.211	11.708	11.123	10.093	(ii)	–	–	–
27	J204227.88+425708.1	310.61618	42.952259	13.673	13.399	12.835	11.614	(iv)	–	–	–
28	J204240.78+425651.6	310.66987	42.947657	12.408	12.079	11.718	11.321	(iv)	1.65	1.03	2.5
29	J204234.29 + 425322.8	310.642883	42.889668	13.897	13.455	13.311	12.41	(iv)	–	–	–
30	J204229.21+425725.4	310.621704	42.957069	12.721	12.174	11.698	10.959	(iv)	–	–	–
31	J204227.65+425728.1	310.615234	42.957802	13.09	12.529	11.956	10.962	(ii)	–	–	–
32	J204229.56+425736.7	310.623138	42.960197	11.516	10.856	10.399	9.889	(iv)	–	–	–
33	J204225.61+425339.2	310.60672	42.894226	13.891	13.461	13.166	12.657	(ii)	–	–	–
34	J204222.72+425413.8	310.594696	42.903831	12.662	12.451	11.961	10.973	(ii)	–	–	–
35	J204226.21+425732.2	310.609222	42.958954	13.338	12.861	12.504	11.539	(ii)	–	–	–
36	J204238.18+425306.8	310.659074	42.885212	11.85	11.304	10.594	9.369	WISE #51 (iv)	1.77	1.09	2.74
37	J204221.45+425345.9	310.589355	42.896095	12.547	11.97	11.307	10.274	WISE #53 (ii)	–	–	–
38	J204215.13+425459.9	310.563049	42.91663	10.705	10.188	9.748	9.203	(ii)	–	–	–
39	J204217.67+425307.6	310.573639	42.885433	13.115	12.469	11.92	10.925	(ii)	–	–	–
40	J204217.15+425226.0	310.571442	42.873898	12.548	11.952	11.595	11.088	(ii)	–	–	–
41	J204215.43+425242.6	310.564301	42.878506	13.241	12.638	12.064	11.329	(ii)	–	–	–
42	J204211.24+425337.2	310.546814	42.893677	10.981	10.787	10.374	10.038	(ii)	–	–	–
43	J204216.26+425048.2	310.567719	42.846733	12.563	11.759	11.127	10.548	(iv)	–	–	–
44	J204209.37+425139.8	310.539032	42.861046	11.286	10.959	10.295	9.863	(ii)	–	–	–
45	J204214.61+425038.0	310.560852	42.843884	13.347	12.491	11.833	11.04	(iv)	–	–	–
46	J204159.01+425535.8	310.49588	42.926624	10.548	9.973	9.47	8.617	WISE #62 (v)	1.77	1.28	2.43
47	J204202.89+425114.2	310.512024	42.853958	13.448	12.791	12.251	11.663	(v)	–	–	–

Based on the Monte Carlo method developed by Wenger et al. (2018), to derive the kinematic distances and uncertainties to the region, we obtained 3.8 ± 0.9, 4.4 ± 0.9 and 4.5 ± 0.9 kpc, respectively, for the three LSR velocities just mentioned. Taking into account the errors introduced when applying a Galactic rotation model in this part of the Galaxy, we concluded that these kinematic distances are in agreement with our estimated distance to the cluster.

4.3.1 Radio continuum emission

Fig. 6 shows the emission distribution of DB2001–22 region at 1420 MHz. Despite the difference in angular resolution regarding the data at 1420 MHz and the IR one presented in Fig. 1, the image clearly distinguishes an arc of intense emission, as well as the most intense spot related to the MSX source G082.5682+00.4040 (indicated by a small circle). The structure is seen open towards the southeast, suggesting that part of the stellar ionizing radiation is escaping from the region while finding denser gas facing the other one.

To estimate the physical parameters of the HII region, such as the amount of ionizing mass (M_{HII}), electron density (n_e) and number of energetic photons needed to keep the region ionized (N_{Lym}), we used the formulae given by Mezger & Henderson (1967) and Chaisson (1976). We estimated the flux density considering different contour levels to define the size of the region and obtained $S_{1420} = 14 \pm 1$ Jy, which is similar to the values found by Normandeau et al. (1992) at 408 and 4850 MHz. Seeing that the ionized gas occupies a spherical volume with radius $\theta_{esp} = 7'.0$ and an electron temperature

Table 5. Continued.

#	Designation	*WISE* sources α (deg.)	δ (deg.)	W1 (mag)	W2 (mag)	W3 (mag)	W4 (mag)	Notes	*Gaia*–dist	lo (kpc)	hi
					Class I						
48	J204224.00+425732.2	310.600011	42.95895	8.988	7.706	4.587	1.838	(iii)	–	–	–
49	J204222.50+425743.2	310.593775	42.962026	10.873	9.213	5.156	2.739	(ii)	–	–	–
					Class II						
50	J204231.63+425627.7	310.631795	42.941034	9.011	8.153	3.936	-1.127	(i)	–	–	–
51	J204238.16+425306.8	310.659035	42.885234	12.023	11.36	8.379	4.485	(iv)	1.77	1.09	2.74
52	J204221.04+425353.0	310.587505	42.898166	11.679	11.34	6.481	3.72	(ii)	2.78	1.99	3.85
53	J204221.49 + 425345.5	310.58956	42.89598	11.67	10.988	6.527	3.495	(ii)	–	–	–
54	J204217.04+425538.5	310.571176	42.927285	11.292	10.695	6.819	3.074	(iii)	1.60	0.72	2.55
55	J204222.54+425759.9	310.593917	42.966644	10.02	9.625	4.957	2.87	(ii)	–	–	–
56	J204222.68+425815.6	310.594519	42.971028	10.703	9.909	5.399	3.075	(ii)	–	–	–
57	J204253.37+425329.6	310.722363	42.891475	13.754	13.144	8.329	3.669	(v)	2.55	1.71	4.14
58	J204212.76+425300.5	310.55318	42.883496	10.644	10.213	5.575	3.437	(iii)	–	–	–
59	J204204.90+425245.4	310.520419	42.879285	12.8	12.254	7.482	4.553	(v)	–	–	–
60	J204214.58+430035.3	310.560516	43.00996	12.428	12.064	7.255	5.307	(v)	1.05	1.01	1.09
61	J204209.68+425056.8	310.540331	42.849122	11.332	10.881	6.757	4.491	(ii)	1.41	1.22	1.59
62	J204159.01+425536.1	310.495895	42.92669	10.583	9.812	7.036	4.321	(v)	1.77	1.28	2.43
63	J204246.44+430121.6	310.693503	43.02268	12.053	11.643	6.782	3.917	(v)	–	–	–
64	J204248.27+430143.2	310.701126	43.028814	12.171	11.851	7.275	4.264	(v)	2.35	2.08	2.71
65	J204252.67+430141.4	310.719583	43.028006	11.934	11.61	7.456	4.868	(v)	7.06	1.95	10.18

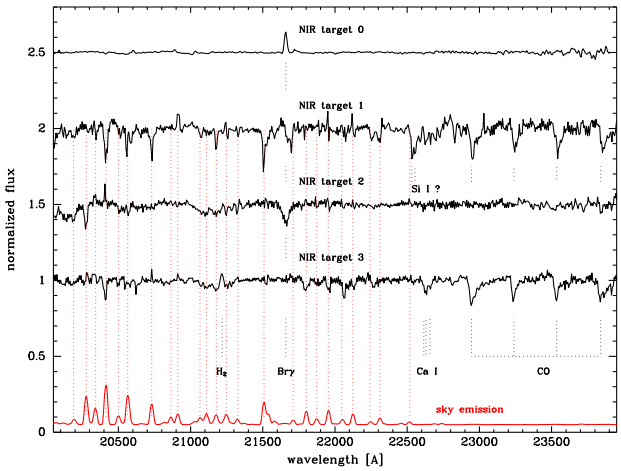

Figure 5. Near IR spectra of the four sources detected in our GNIRS observations. Most intense sky emissions, in red, are also indicated with vertical lines.

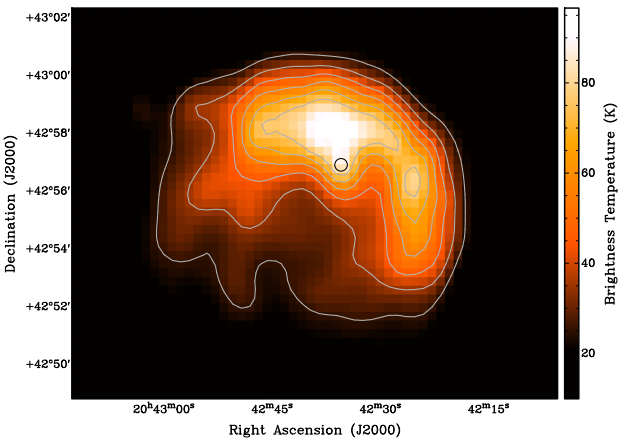

Figure 6. 1420 MHz image of the HII region G82.6+0.4. Contour levels are from 25 to 75 K in step of 10 K. The small black circle indicates the location of the MSX source G082.5682+00.4040.

$T_e = 8030 \pm 128$ K (Balser et al. 2011), we estimated a $M_{HII} = 1225 \pm 480\ M_\odot$, $n_e = 33 \pm 6\ cm^{-3}$ and $N_{Lym} = (1.5 \pm 0.4) \times 10^{49}\ s^{-1}$. For this calculation we adopted the average distance derived from Section 4.1, i.e. 3.0 ± 0.4 kpc, given that those results were performed applying more reliable techniques than the ones used to calculate kinematic distances.

Taking into account the presence of the O7 V star, and assuming that the O6 IIIz is also powering this region, (see distances in Table 4 and Section 4.1), they would provide 5×10^{48} and 2×10^{49} ph s^{-1}, respectively (Martins, Schaerer & Hillier 2005). Thus, together, they contribute about 60 per cent more than the number of photons needed for the region to be ionized.

4.3.2 Infrared emission

As mentioned in Section 1 and shown in Fig. 1, the region is very conspicuous in the mid-IR.

Fig. 7 shows the emission distribution at three mid-IR bands mapping different dust components. The one at 24 -μm (in red), which maps warm dust, is seen in the interior of the cavity, where the stellar radiation is high. Emission at this band is also evident at the location of the MSX source G082.5682+00.4040, which, since it is mixed with the 8 μm emission (in green), is seen in yellow. The one at 8 μm delineates the photo-dissociation region (PDR) due to emission from bending/stretching modes of PAHs excited by the ultraviolet (UV) radiation, and characterize the interface area between the ionized gas and the cold molecular cloud. Several arc and pillar structures are evident at 8 μm , being the one that contains G082.5682+00.4040 in its tip, the most striking one. Finally, the emission at 4.5 μm (in blue) shows the IR emission originated in the stellar photospheres.

All the observed emission distributions points out to the presence of hot ionized gas mixed with warm dust partially surrounded by a well-structured PDR, indicating the presence of molecular gas where star formation could be taking place as a consequence of the action of the massive stars present inside the cavity.

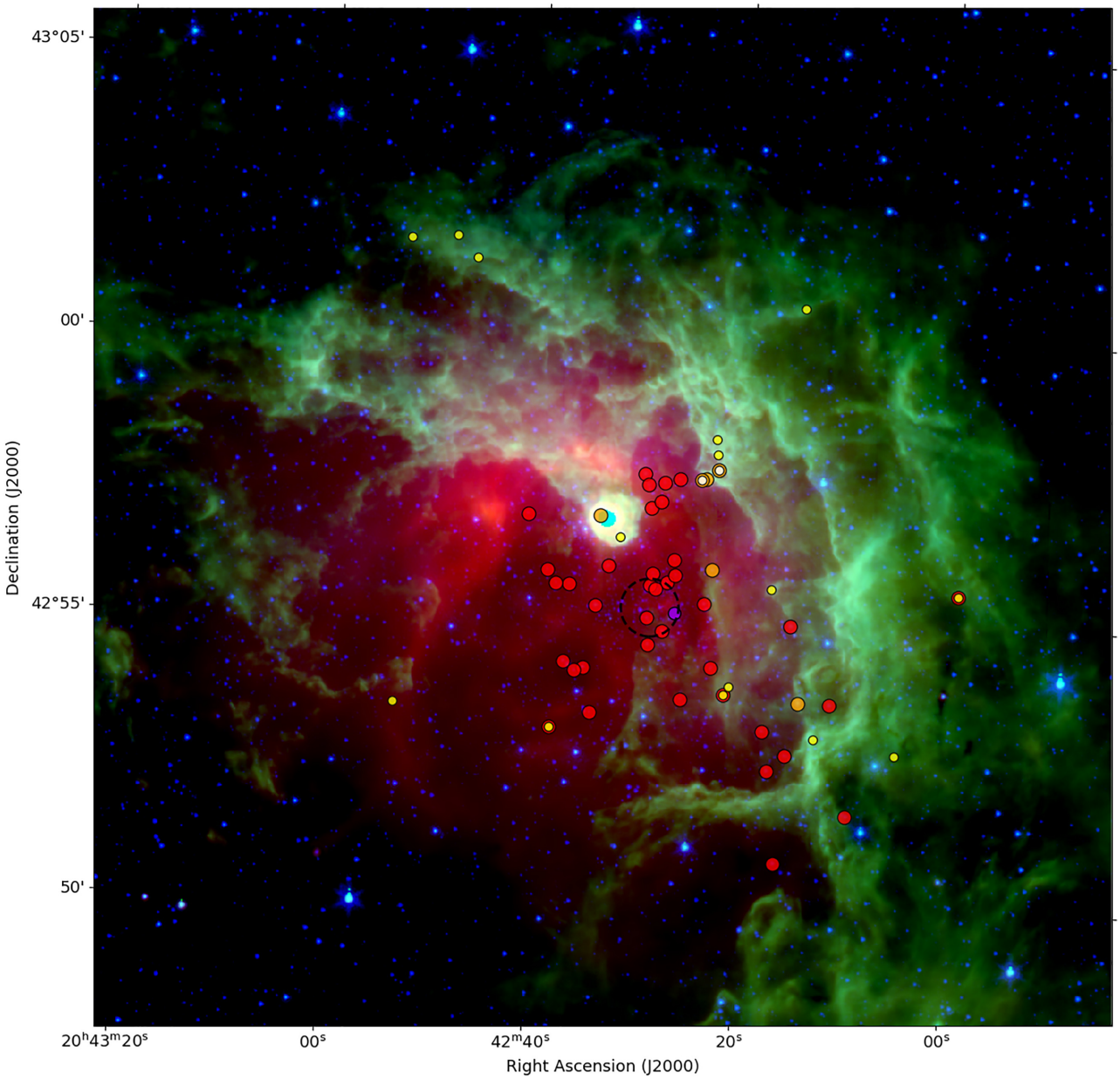

Figure 7. Colour composite image centred in the DB2001–22 position covering a region of 18 × 18 arcmin, showing the emission corresponding to three *Spitzer* bands: colour red traces MIPS 24 μm emission, while green and blue trace the IRAC 8 and 4.5 μm emission, respectively. The orange and red circles indicate the location of *WISE* Class I and Class II candidate sources, respectively, while the white and yellow ones indicate *Spitzer* Class I and Class II candidate sources, respectively. The dashed black circle shows the location of a small group of stars (see Fig. 1), where the violet filled circle inside it indicates the one that is a massive star candidate.

Using *Herschel* data corresponding to the wavelength range 70–500 μm and the PPMAP (Point Process Mapping) algorithm, Marsh et al. (2017) obtained integrated column densities and mean dust temperatures maps of the Galactic Plane. One important advantage of this new procedure over the previously used is that the derived images have a high resolution of 12 arcsec. Fig. 8 shows the dust temperature distribution in the region under study. It can be seen that the temperature is about 20–21 K in most part of the region and reaches its maximum of around 30 K in the location of G082.5682+00.4040, suggesting the presence of a source that has already started to heat the dust in its environs.

5 DISCUSSION

The location of the cYSOs (see Fig. 7) points out that they are mainly distributed in five different zones: (i) two are located on to the bright IR source, (ii) several can be seen projected on to different parts of the PDR, (iii) some are located at the tips of pillars pointing into the cavity, (iv) several are inside the cavity, and (v) a few are located in the most external part of the PDR, far from the interior of the cavity. Column 9 of Table 5 indicates which of these groups each source belongs to.

To firmly associate the detected cYSOs with the H II region, we looked for their *Gaia* eDR3 source counterparts. We found distance

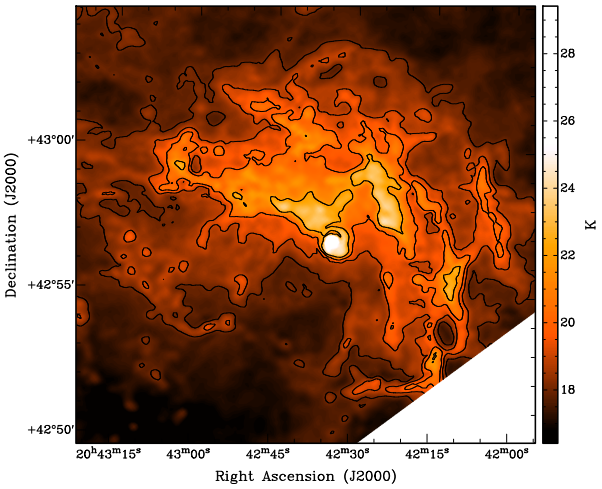

Figure 8. Dust temperature distribution derived from *Herschel* data. Contour levels are at 18, 19, 20, and 22 K.

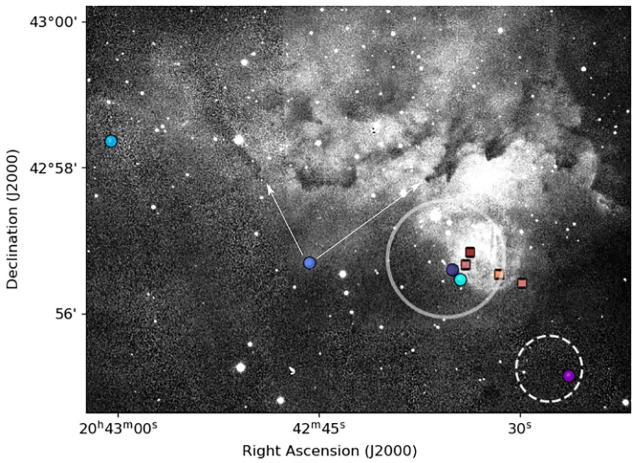

Figure 9. IPHAS images in the Hα band. We show the orientation of two pillar-like structures, respect the position of the O7 V source. Symbols and circles have the same meaning as in Fig. 1.

information for 22 out of the 65 cYSOs (see Table 5), 13 of them have distances compatible with the 3 kpc of the cluster.

An inspection of the cYSOs distribution suggests that their formation may have been induced by the action of the earliest stars in the cluster. In particular, the large amount of cYSOs located on the PDR (22 out of 65) is striking. Since the presence of a PDR is a clear proof of the interaction between the ionized region and the molecular gas, the relative location of the cYSOs with respect to the PDR may be considered as an indication of the role that the H II region is playing in the formation of the new stars. The probability for a source of being triggered by the action of massive stars upon the ISM is higher when it is located within the region of direct influence of them.

The induced star-formation process known as 'collect and collapse' (C&C) may be taking place in the region (Elmegreen & Lada 1977). In particular, this process could be the one that took place in the formation of the cYSOs located on the PDR. In turn, the sources located at the tips of the pillars have a high probability of having been formed by the radiation-driven implosion mechanism (RDI), which favours the formation of cometary globules in pre-existent clumps and the formation of new stars inside them (Lefloch & Lazareff 1994). This is probably the case for the formation of the source named target 0. The cometary shape that presents the structure where this source is located, is facing the small group of stars, identified as the second peak in our stellar density map analysis (indicated in Figs 1 and 7 by a dashed black circle). Particularly, as mentioned above, within this small group, we identified an early-type star candidate, 2MASS J20422635+4255099, indicated in both figures with a filled violet circle. The location of this group of stars, and the calculated distances of this particular source (3.1 ± 0.3 kpc), with respect to the cometary structure, is where one would expect to find the responsible for this kind of structure hosting new stellar objects.

Finally, we see that several cYSOs apparently fall into the cavity. Since all of them are classified as class II sources, their location may indicate that either they have already moved away from the place where they were formed or that they already dissipated it. The presence of this group of young stars was already pointed out by Beerer et al. (2010, see their fig. 15).

Additionally, in Fig. 9, we present an image showing the Hα (Drew et al. 2005) emission distribution in a region that partially covers the studied area (see Fig. 1). The DB2001–22 cluster is seen projected on to the region where the optical emission appears to be highest. Several pillar-like structures, seen in absorption against high emission, are striking in this image. Both the morphology and orientation of these two structures suggest that the strong radiation provided by the O7 V star could be the responsible for their formation.

6 CONCLUSIONS

By means of a multiple technique analysis, we studied the region that encompass DB2001–22. We were able to identify the different stellar components and derived its distance, colour excess, and age. In turn, we addressed their relation to the observed ISM structures.

The distance was independently determined by applying three methods. We obtained same values with slightly different errors and adopted a mean distance of 3.0 ± 0.4 kpc. Thus, the cluster is further away than the Cygnus–X region and the Cyg–OB2 association, i.e. not related.

We applied spectroscopic/photometric calculations and estimations to derived the colour excess and found a normal absorption behaviour for the ISM. In both cases, and taking into account the calculations applied to the optical and near-IR photometric bands in all four OB stars, we concluded an $E_{(B-V)} = 1.9$ ($A_V = 5.9$).

The age of the cluster was established using the presence of a O7 V star and by contrasting a set of isochrones to photometric data. Thus, we inferred an upper limit range of 8–10 Myr.

We identified an additional O7–7.5 V type star in the LAMOST spectral data base. We downloaded the spectrum and identified He II (among others, see Section 4.1.1) features which led us to classify it as such. Other spectrum identified as A0 III in the data base was reclassified as B3 V. The spectral LAMOST data base could harbour others hitherto unveiled early-type stars.

We analysed the distribution and characteristics of the gas and dust present in the DB2001–22 surroundings. Using radio continuum data, we found that two O-type stars in the region supply the needed energetic photons, even taking into account that part of it may escape from the region, specially from its open border, and the rest is used to heat the dust. However, the possible contribution to the ionizing photon budget of the small group of stars, indicated with a dash–black circle in Fig. 2, as well as others still not detected massive stars, cannot be discarded. The distribution of the IR emission is clearly compatible with the scenario of hot ionized gas mixed with

warm dust partially surrounded by a well-structured PDR, indicating the presence of molecular gas where star-formation could be taking place as a consequence of the action of the massive stars present inside the cavity.

From a visual inspection of Hα images, pillar-like structures were identified. Two of them point towards the O7 V type star. Regarding these findings and the IR emission distribution, the relationship between DB2001–22 and the ISM structures is clearly confirmed. We have also searched for cYSOs trying to characterize the stellar forming region. We pointed GNIRS/Gemini at sources with near-IR excesses. We obtained a spectrum of the MSX source G082.5682+00.404, but no other feature than Brγ in emission was detected. The remaining sources were classified as K0 giants (the third spectrum corresponded to a foreground A-type star), with no distinguishable emissions. These stars have geometric distances determined which, although with large errors and with exception to target 2, all other three are situated at the clusters distance, nevertheless we discard them as members. We also took advantage of the *WISE* and *Spitzer* data bases. We found 9 IR sources identified as Class I and 56 as Class II cYSOs (one of them coincident with the MSX source G082.5682+00.404). In a rough analysis, several Class II candidates are located in the cavity and Class I (i.e. more recent ones), in the PDR. Moreover, some Class I candidates are located at the tips of pillars, which in turn point into the cavity where massive stars are placed. Triggered star formation may be taking place in the region, i.e. the expanding shock produced by the expansion of the H II region sweeps the surrounding material and produces gravitational instabilities.

Finally, the DB2001–22 embedded cluster and its environment, is much richer than already considered, i.e. it comprises several massive stars inducing the formation of a new stellar generation. Upon the results for distances obtained from the stellar components, and the calculation performed to derive kinematic distances (see Section 4.3), as well as the morphology of the ISM relative to the position of massive stars, we conclude that the cluster, the pillar and the bubble structure are related and situated at 3.0 $\pm$ 0.4 kpc. Moreover, the stellar density analysis shows a second smaller cluster, which deserves further attention, that could be related to the star-formation processes inside the knot.

ACKNOWLEDGEMENTS

This research has made use of the SIMBAD data base, operated at CDS, Strasbourg, France. This publication was based on: (i) observations obtained at the international Gemini Observatory, a program of NSF's NOIRLab, which is managed by the Association of Universities for Research in Astronomy (AURA) under a cooperative agreement with the National Science Foundation. on behalf of the Gemini Observatory partnership: the National Science Foundation (United States), National Research Council (Canada), Agencia Nacional de Investigación y Desarrollo (Chile), Ministerio de Ciencia, Tecnología e Innovación (Argentina), Ministério da Ciência, Tecnologia, Inovações e Comunicações (Brazil), and Korea Astronomy and Space Science Institute (Republic of Korea). (ii) the 2MASS, which is a joint project of the University of Massachusetts and the IPAC / California Institute of Technology, funded by the NASA and the NSF; (iii) data products from the *WISE*, which is a joint project of the University of California, Los Angeles and the JPL / California Institute of Technology, and is funded by the NASA; (iv) 'A *Spitzer* Legacy Survey of the Cygnus–X Complex', a project to survey a 24 deg^2 region with the IRAC 3.6, 4.5, 5.8, and 8.0μm bands and MIPS 24 and 70 μm bands to study a relatively nearby active region of massive star formation; (v) data from the ESA mission *Gaia*, processed by the *Gaia* DPAC. Funding for the DPAC has been provided by national institutions, in particular the institutions participating in the *Gaia* Multilateral Agreement; (vi) Guoshoujing Telescope (the Large Sky Area Multi-Object Fiber Spectroscopic Telescope LAMOST), which is a National Major Scientific Project built by the Chinese Academy of Sciences. Funding for the project has been provided by the National Development and Reform Commission. LAMOST is operated and managed by the National Astronomical Observatories, Chinese Academy of Sciences, and (vii) radio continuum data from the CGPS, which is a Canadian project with international partners and is supported by grants from NSERC. Data from the CGPS are publicly available through the facilities of the Canadian Astronomy Data Centre (http://cadc.hia.nrc.ca) operated by the Herzberg Institute of Astrophysics, NRC. JA:M-L, RG, and GB acknowledge support from CONICET grant PIP 112-201701-00055 and PICT 2019-0344. SC and SBC acknowledge support from CONICET grant PIP 112-201701-00604 (Argentina). RG acknowledges support of the UNLP project 80120180200065LP.

DATA AVAILABILITY

The data underlying this article are available at the Centre de Données astronomiques de Strasbourg (CDS[9]). It also can be shared on reasonable request to the corresponding author.

REFERENCES

Alam S. et al., 2015, ApJS, 219, 12
Anderson L. D., Bania T. M., Balser D. S., Cunningham V., Wenger T. V., Johnstone B. M., Armentrout W. P., 2014, ApJS, 212, 1
Bailer-Jones C. A. L., Rybizki J., Fouesneau M., Demleitner M., Andrae R., 2021, AJ, 161, 147
Balser D. S., Rood R. T., Bania T. M., Anderson L. D., 2011, ApJ, 738, 27
Baume G., Carraro G., Comeron F., de Elía G. C., 2011, A&A, 531, A73
Baume G., Corti M. A., Borissova J., Ramirez Alegria S., Corvera A. V., 2020, New Astron., 79, 101384
Beerer I. M. et al., 2010, ApJ, 720, 679
Berlanas S. R., Herrero A., Comerón F., Pasquali A., Bertelli Motta C., Sota A., 2018, A&A, 612, A50
Berlanas S. R. et al., 2020, A&A, 642, A168
Bica E., Dutra C. M., Barbuy B., 2003, A&A, 397, 177
Bochkarev N. G., Sitnik T. G., 1985, Ap&SS, 108, 237
Bressan A., Marigo P., Girardi L., Salasnich B., Dal Cero C., Rubele S., Nanni A., 2012, MNRAS, 427, 127
Cantat-Gaudin T. et al., 2018, A&A, 618, A93
Cardelli J. A., Clayton G. C., Mathis J. S., 1989, ApJ, 345, 245
Chaisson E. J., 1976, in Avrett E. H., ed., Frontiers of Astrophysics. Harvard Univ. Press, Cambridge, p. 259
Chambers K. C. et al., 2016, preprint (arXiv:1612.05560)
Cichowolski S., Suad L. A., Pineault S., Noriega-Crespo A., Arnal E. M., Flagey N., 2015, MNRAS, 450, 3458
Cichowolski S., Duronea N. U., Suad L. A., Reynoso E. M., Dorda R., 2018, MNRAS, 474, 647
Brown A. G. A., Vallenari A., Prusti T., de Bruijne J. H. J., Babusiaux C., Biermann M., Collaboration G., 2021, A&A , 650, C3
Cutri R. M. et al., 2012, Explanatory Supplement to the WISE All-Sky Data Release Products. p. 1
Doppmann G. W., Greene T. P., Covey K. R., Lada C. J., 2005, AJ, 130, 1145
Drew J. E. et al., 2005, MNRAS, 362, 753
Dutra C. M., Bica E., 2001, A&A, 376, 434
Eisenstein D. J. et al., 2011, AJ, 142, 72

[9]http://simbad.u-strasbg.fr/simbad/

Ekström S. et al., 2012, A&A, 537, A146
Elmegreen B. G., Lada C. J., 1977, ApJ, 214, 725
Gehrz R. D. et al., 1980, AJ, 85, 1071
Ghosh S., Mondal S., Das R., Khata D., 2019, MNRAS, 484, 4619
Greene T. P., Lada C. J., 1996, AJ, 112, 2184
Gutermuth R. A., Megeath S. T., Myers P. C., Allen L. E., Pipher J. L., Fazio G. G., 2009, ApJS, 184, 18
Hanaoka M. et al., 2019, PASJ, 71, 6
Hora J. et al., 2007, A Spitzer Legacy Survey of the Cygnus-X Complex, Spitzer Proposal
Hou L. G., Han J. L., 2014, A&A, 569, A125
Ishii M., Nagata T., Sato S., Yao Y., Jiang Z., Nakaya H., 2001, AJ, 121, 3191
Jester S. et al., 2005, AJ, 130, 873
Kharchenko N. V., Piskunov A. E., Schilbach E., Röser S., Scholz R.-D., 2013, A&A, 558, A53
Kimeswenger S., Barría D., 2018, A&A, 616, L2
Koenig X. P., Leisawitz D. T., Benford D. J., Rebull L. M., Padgett D. L., Assef R. J., 2012, ApJ, 744, 130
Koornneef J., 1983, A&AS, 51, 489
Lefloch B., Lazareff B., 1994, A&A, 289, 559
Lockman F. J., 1989, ApJS, 71, 469
Lumsden S. L., Hoare M. G., Urquhart J. S., Oudmaijer R. D., Davies B., Mottram J. C., Cooper H. D. B., Moore T. J. T., 2013, ApJS, 208, 11
Marsh K. A. et al., 2017, MNRAS, 471, 2730
Martins F., Schaerer D., Hillier D. J., 2005, A&A, 436, 1049
Meyer M. R., Calvet N., Hillenbrand L. A., 1997, AJ, 114, 288
Meynet G., Mermilliod J. C., Maeder A., 1993, A&AS, 98, 477
Mezger P. G., Henderson A. P., 1967, ApJ, 147, 471
Molina Lera J. A., Baume G., Gamen R., 2018, MNRAS, 480, 2386
Molina Lera J. A., Baume G., Gamen R., 2019, MNRAS, 488, 2158
Motte F., Bontemps S., Schilke P., Schneider N., Menten K. M., Broguière D., 2007, A&A, 476, 1243
Normandeau M., Joncas G., Green D. A., 1992, A&AS, 92, 63
Odenwald S. F., Schwartz P. R., 1993, ApJ, 405, 706
Oskinova L. M., Gruendl R. A., Ignace R., Chu Y. H., Hamann W. R., Feldmeier A., 2010, ApJ, 712, 763
Piddington J. H., Minnett H. C., 1952, Austr. J. Sci. Res. A Phys. Sci., 5, 17
Rayner J. T., Cushing M. C., Vacca W. D., 2009, ApJS, 185, 289
Reid M. J. et al., 2019, ApJ, 885, 131
Reipurth B., Schneider N., 2008, Star Formation and Young Clusters in Cygnus. p. 36
Schneider N., Bontemps S., Simon R., Jakob H., Motte F., Miller M., Kramer C., Stutzki J., 2006, A&A, 458, 855
Shen J., Zheng X.-W., 2020, Res. Astron. Astrophys., 20, 159
Skrutskie M. F. et al., 2006, AJ, 131, 1163
Stetson P. B., 1987, PASP, 99, 191
Stetson P. B., 1992, in Worrall D. M., Biemesderfer C., Barnes J., eds, ASP Conf. Ser. Vol. 25, Astronomical Data Analysis Software and Systems I. Astron. Soc. Pac., San Francisco, p. 297
Stoughton C. et al., 2002, AJ, 123, 485
Sung H., Lim B., Bessell M. S., Kim J. S., Hur H., Chun M.-Y., Park B.-G., 2013, J. Korean Astron. Soc., 46, 103
Taylor A. R. et al., 2003, AJ, 125, 3145
Urquhart J. S. et al., 2009, A&A, 501, 539
Walborn N. R., Fitzpatrick E. L., 1990, PASP, 102, 379
Wallace L., Hinkle K., 1997, ApJS, 111, 445
Wendker H. J., 1970, A&A, 4, 378
Wendker H. J., 1984, A&AS, 58, 291
Wenger T. V., Balser D. S., Anderson L. D., Bania T. M., 2018, ApJ, 856, 52
Zari E., Rix H. W., Frankel N., Xiang M., Poggio E., Drimmel R., Tkachenko A., 2021, A&A, 650, A112

This paper has been typeset from a TEX/LATEX file prepared by the author.